Supporting Information

N-doped branched metal-organic framework derivatives to boost multiband microwave absorption with ultrathin thickness

Zhe Zhang,[a] Jiewu Cui,*[a] Dongbo Yu,*[a] Jiaqin Liu,[b] Pengjie Zhang,[c] Yong Zhang,[a] Song Ma,[d] Linjie Wang,[e] Guangsheng Deng[e] and Yucheng Wu*[a]

[a] School of Materials Science and Engineering, Key Laboratory of Advanced Functional Materials and Devices of Anhui Province, Hefei University of Technology, Hefei 230009, China

[b] Institute of Industry & Equipment Technology, Engineering Research Center of Advanced Composite Materials Design & Application of Anhui Province, Hefei University of Technology, Hefei 230009, China

[c] BGRIMM Technology Group Co, Ltd, Beijing 102600, China

[d] Shenyang National Laboratory for Materials Science, Institute of Metal Research, Chinese Academy of Sciences, Shenyang 110016, China

[e] Academy of Opto-electric Technology, Hefei University of Technology, Hefei 230009, China

Corresponding authors. E-mail: jwcui@hfut.edu.cn, dongboy@hfut.edu.cn, ycwu@hfut.edu.cn

Experimental section

Materials

2,5-dihydroxyterephthalic acid (DHTA, ≥ 99%), cobalt chloride hexahydrate ($CoCl_2 \cdot 6H_2O$, ≥ 99%), nickel chloride hexahydrate($NiCl_2 \cdot 6H_2O$, ≥ 99%), sodium hydroxide (NaOH, ≥ 99%), ethanol (purity ≥ 99.7%), melamine ($C_3H_6N_6$, ≥ 99%) were purchased from Sinopharm Chemical Reagent Co., Ltd. All chemicals are chemically pure without subsequent purification. Deionized water is acquired directly from our laboratory(electrical resistivity ~ 18.2 MΩ·cm).

Synthesis of CoNi-MOF-74 nanorods.

Co/Ni-MOF-74 nanorods were prepared according to the previous reported method with slight modifications [1, 2]. 2 mmol $CoCl_2 \cdot 6H_2O$ and 2 mmol $NiCl_2 \cdot 6H_2O$ were dissolved in 10 ml of deionized water. Subsequently, 2mmol DHTA and 4.5 mmol NaOH (adjusting the pH of the solution to trap the protons in DHTA, enabling DHTA to form water-soluble ionic compounds) were dispersed into 90 ml deionized water. Afterward, the two solutions are mixed and continuously stirred at 100 °C for 1 h. Finally, the CoNi-MOF-74 was collected through centrifugation, washing by ethanol, and drying at 60 °C for 24 h. For comparison, the synthesis processes of Co-MOF-74 (4 mmol $CoCl_2 \cdot 6H_2O$) nanorods and Ni-MOF-74 (4 mmol $NiCl_2 \cdot 6H_2O$) nanorods were conducted in a manner similar to that of CoNi-MOF-74.

Synthesis of CoNi@PC/CNTs composites.

CoNi@PC/CNTs was synthesized via pyrolysis. The CoNi-MOF-74 nanorods product was pyrolysis under Ar atmosphere in a tube furnace at 600 °C for 2 h with a heating rate of 2 °C/min, ultimately resulting in the formation of CoNi@PC/CNTs. Following a procedure similar to that used for CoNi@PC/CNTs, the pyrolysis products of Co-MOF-74 and Ni-MOF-74 were denoted as Co@PC and Ni@PC/CNTs.

Synthesis of CoNi@NPC/NCNTs composites.

CoNi@NPC/NCNTs was fabricated by melamine-assisted chemical vapor deposition pyrolysis. Two quartz boats containing CoNi-MOF-74 and melamine powder, with a weight ratio of 1:5, were inserted into the tube furnace. Notably, the melamine powder was positioned upstream within the tube, while CoNi-MOF-74 was located downstream. Under the heating rate of 2 °C/min, CoNi-MOF-74 was pyrolysis at 700 °C for 2 h under an Ar atmosphere. The obtained black powder samples are designated as CoNi@NPC/NCNTs. Following a procedure similar to that used for CoNi@NPC/NCNTs, the pyrolysis products of Co-MOF-74 and Ni-MOF-74 are denoted as Co@NPC/NCNTs and Ni@NPC/NCNTs.

Characterization

The morphology, microstructure and elemental information of the as-prepared samples were characterized by field emission scanning electron microscopy (SEM, Regulus 8230), transmission electron microscopy (TEM, JEM-1400flash), field-emission transmission electron microscopy (FETEM, JEM-2100F), and transmission electron microscopy (TEM, Talos F200X G2) with energy dispersive X-rays spectroscopy (EDX). The crystal structures of samples were analyzed via X-ray diffractometry with a scanning range of $5° < 2\theta < 80°$ (XRD, Rigaku D/MAX2500VL/PC). Raman spectroscopy was employed to reveal the degree of graphitization (LabRAM HR Evolution). Surface element valence states and chemical bonds were analyzed by X-ray photoelectron spectroscopy (XPS, ESCALAB 250Xi). The magnetic properties of samples were measured by vibrating sample magnetometer (VSM, LakeShore 7404). Physisorption analyzer. (Autosorb-IQ3) to obtain Brunauer-Emmett-Teller (BET) surface areas and pore size distribution of samples.

Microwave Absorption Measurements

The as-prepared Co@PC, CoNi@PC/CNTs, Ni@PC/CNTs, Co@NPC/NCNTs, CoNi@NPC/NCNTs, and Ni@NPC/NCNTs composites were uniformly mixed with paraffin wax in a mass ratio of 1:3. Following the theory of coaxial line and waveguide methods to press them into toroidal-shaped samples (outer diameter: 7.00 mm, inner diameter: 3.04 mm, and thickness: 2.0 mm) and cuboid-shaped samples (length: 7.20 mm, width: 3.60 mm, and thickness: 2.0 mm). The electromagnetic parameters of composites were analyzed in the ranges of 2–18 GHz and 26.5–40 GHz using a network vector analyzer (ROHDE&SCHWARZ ZNA43).

Radar Cross Section (RCS) Simulation

The RCS distribution of CoNi@NPC/NCNTs was simulated using CST Studio Suite 2019. The solving frequency was selected as 14.16 and 32.81 GHz for the dual-band. Build a composite double-layer board model (Figure S10) composed of an absorber layer and a perfect conductive layer with dimensions of 200 × 200 mm. The thickness of the absorber layer is 1.6 and 0.7 mm, corresponding to 14.16 and 32.81 GHz, respectively. The double-layer board simulation model is placed on the x-o-y plane, and the planar electromagnetic wave is incident from the positive direction of the Z-axis to the negative direction of the z-axis. Using the open (with space) boundary conditions in this direction, the scattering direction is determined by θ and φ. The value of RCS can be expressed using the following formula [3]:

$$\sigma\left(dB\,m^2\right) = 10\log\left(\frac{4\pi S}{\lambda^2}\left|\frac{E_s}{E_i}\right|^2\right) = 10\log\left(\frac{4\pi S}{\lambda^2}\left|\frac{H_s}{H_i}\right|^2\right)$$

where, S and λ represent the area of the simulation model and the wavelength of the incident EMW, E_s and E_i represent the electric field intensity of the received scattered wave and the electric field intensity of incident wave, and H_s and H_i represent the magnetic field intensity of the received scattered wave and the magnetic field intensity of incident wave.

Equations

The reflection loss (RL) value can be calculated based on the transmission line theory by equation S1 and equation S2 [4].

$$Z_{in} = Z_0\sqrt{\mu_r/\varepsilon_r}\tan\left[j(2\pi f d/c)\sqrt{\mu_r\varepsilon_r}\right] \quad \text{(S1)}$$

$$RL(dB) = 20\log\left|\left(Z_{in} - Z_0\right)/\left(Z_{in} + Z_0\right)\right| \quad \text{(S2)}$$

where, Z_0 and Z_{in} denote the free-space impedance ($Z_0 \approx 377\ \Omega$) and the input impedance, ε_r and μ_r denote the negative permittivity and complex permeability, and *f*, *d*, and *c* represent frequency of EMW, thickness of absorber, and speed of light, respectively.

According to Debye theory, if the Cole–Cole curve (ε″ vs. ε′) is a typical semicircle (equation S3), it indicates the existence of a Debye relaxation process within the material [5].

$$(\varepsilon' - \frac{\varepsilon_s + \varepsilon_\infty}{2})^2 + (\varepsilon'')^2 = \left(\frac{\varepsilon_s - \varepsilon_\infty}{2}\right)^2 \quad \text{(S3)}$$

According to equation S4 and S5 , intrinsic magnetic permeability (μ_i, μ'') is closely related to magnetic properties [6].

$$\mu_i = \frac{M_s^2}{akH_cM_s + b\lambda\xi} \quad \text{(S4)}$$

$$\mu'' = 2\pi\mu_0(\mu')^2\sigma d^2 f/3 \quad \text{(S5)}$$

where, M_s and H_c are the saturation magnetization and coercive force, a and b are two constants determined by material, λ is the magnetostriction constant, ξ is the elastic strain parameter of the crystal, and μ_0 is the vacuum permeability.

As the frequency increases, if the C_0 value remains stable, it means there is eddy current loss, might be described by equation S6 [7]：

$$C_0 = \mu''(\mu')^{-2}f^{-1} \quad \text{(S6)}$$

The quarter-wavelength cancellation model is based on the interference theory, which is complementary to the impedance matching theory and has universal applicability. According to equation S7 [8]:

$$t_m = \frac{n\lambda}{4} = \frac{nc}{4f_m\sqrt{|\mu_r||\varepsilon_r|}}\ (n = 1, 3, 5, 7 \cdots) \quad \text{(S7)}$$

where c is the speed of light, t_m is the thickness of the simulated absorber, and f_m is the frequency corresponding to the lowest reflection loss.

Attenuation constant (α) is appointed to evaluate the attenuation capability (equation S8) [9].

$$\alpha = \frac{\sqrt{2}\pi f}{c}\sqrt{(\mu''\varepsilon'' - \mu'\varepsilon') + \sqrt{(\mu''\varepsilon'' - \mu'\varepsilon')^2 + (\mu'\varepsilon'' + \mu''\varepsilon')^2}} \quad \text{(S8)}$$

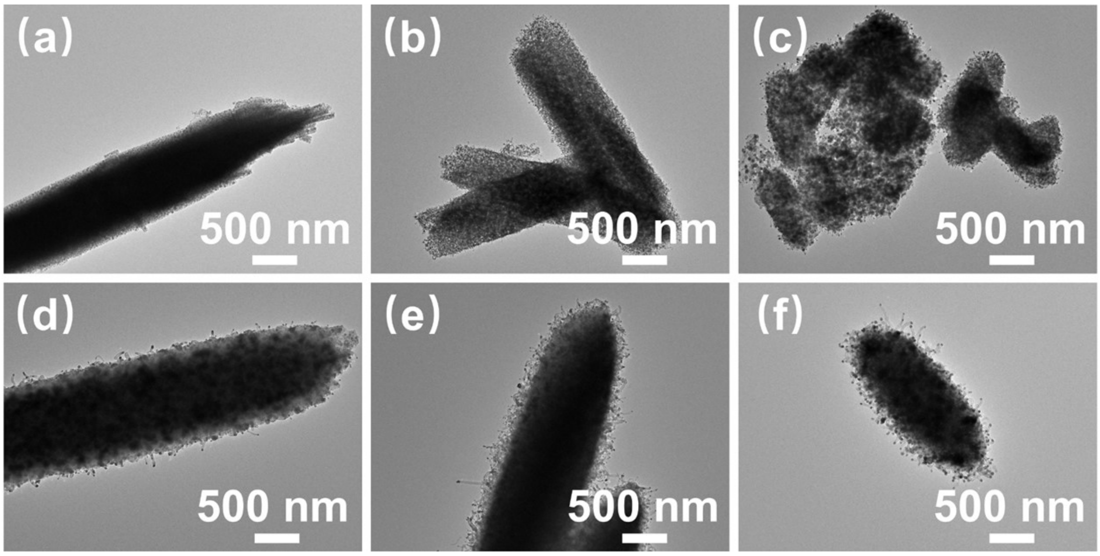

Figure S1. a-f) TEM images of Co@PC, CoNi@PC/CNTs, Ni@PC/CNTs, Co@NPC/NCNTs, CoNi@NPC/NCNTs, and Ni@NPC/NCNTs.

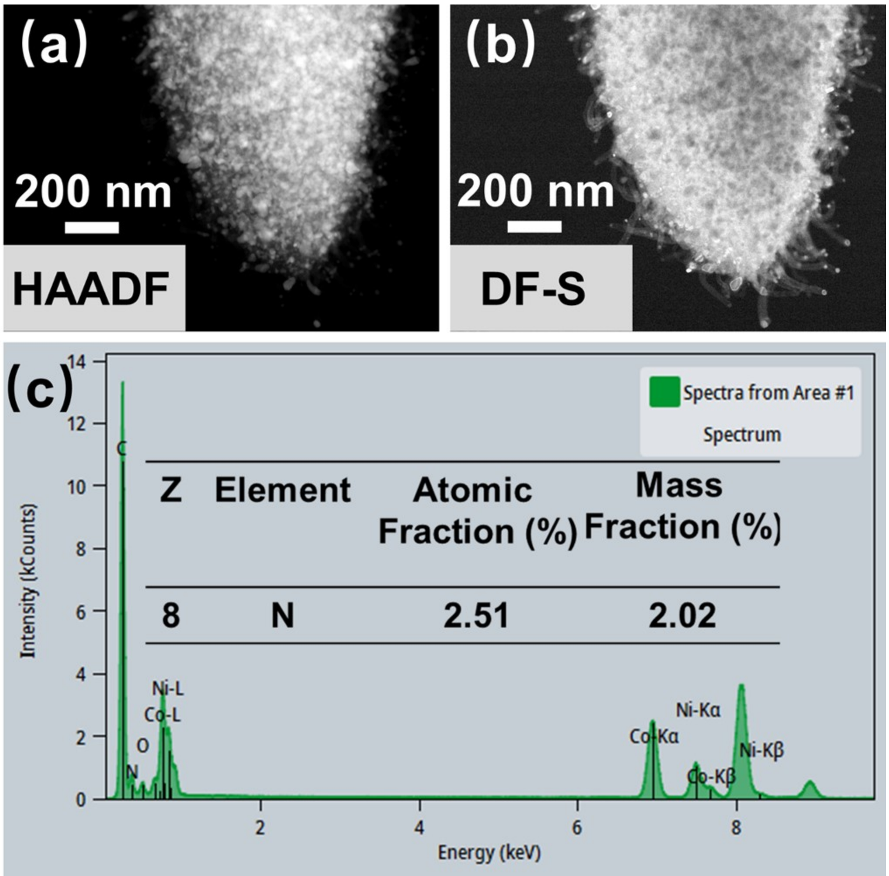

Z	Element	Atomic Fraction (%)	Mass Fraction (%)
8	N	2.51	2.02

Figure S2. a) HAADF image, b) DF-S image, and c) EDX spectra of CoNi@NPC/NCNTs. Table in Figure S2c is the N element of atomic fraction and mass fraction.

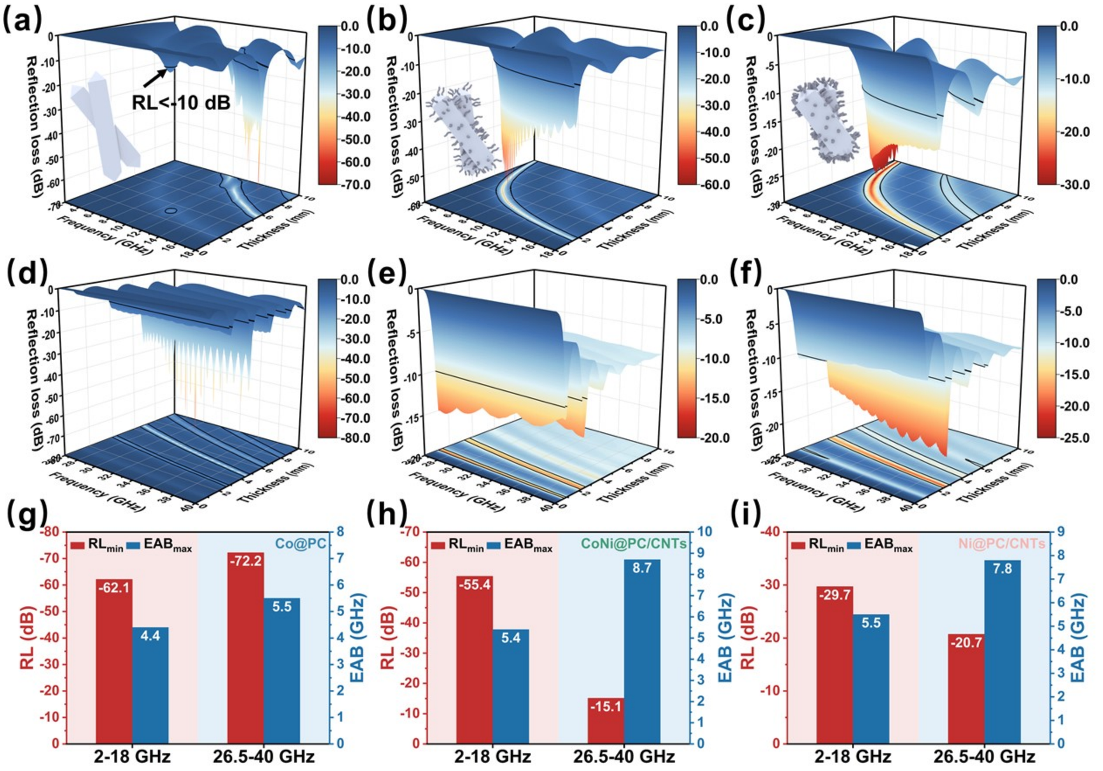

Figure S3. 3D RL curves of a, d) Co@PC, b, e) CoNi@PC/CNTs, and c, f) Ni@PC/CNTs in the ranges of 2–18 and 26.5–40 GHz, respectively. g-i) RL_{min} and EAB_{max} comparison of Co@PC, CoNi@PC/CNTs, and Ni@PC/CNTs in the ranges of 2–18 and 26.5–40 GHz, respectively.

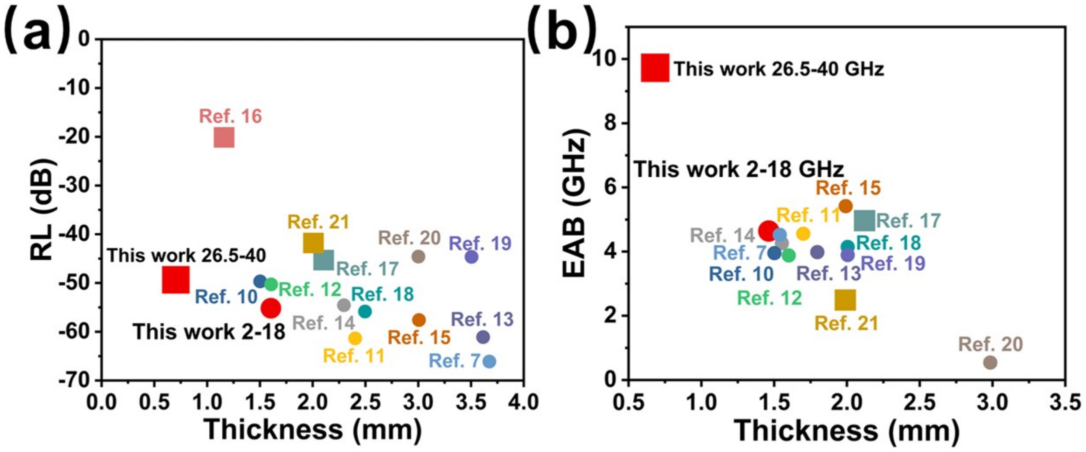

Figure S4. Comparison of the performance for previously reported materials with electromagnetic wave absorption properties : a) RL, b) EAB.

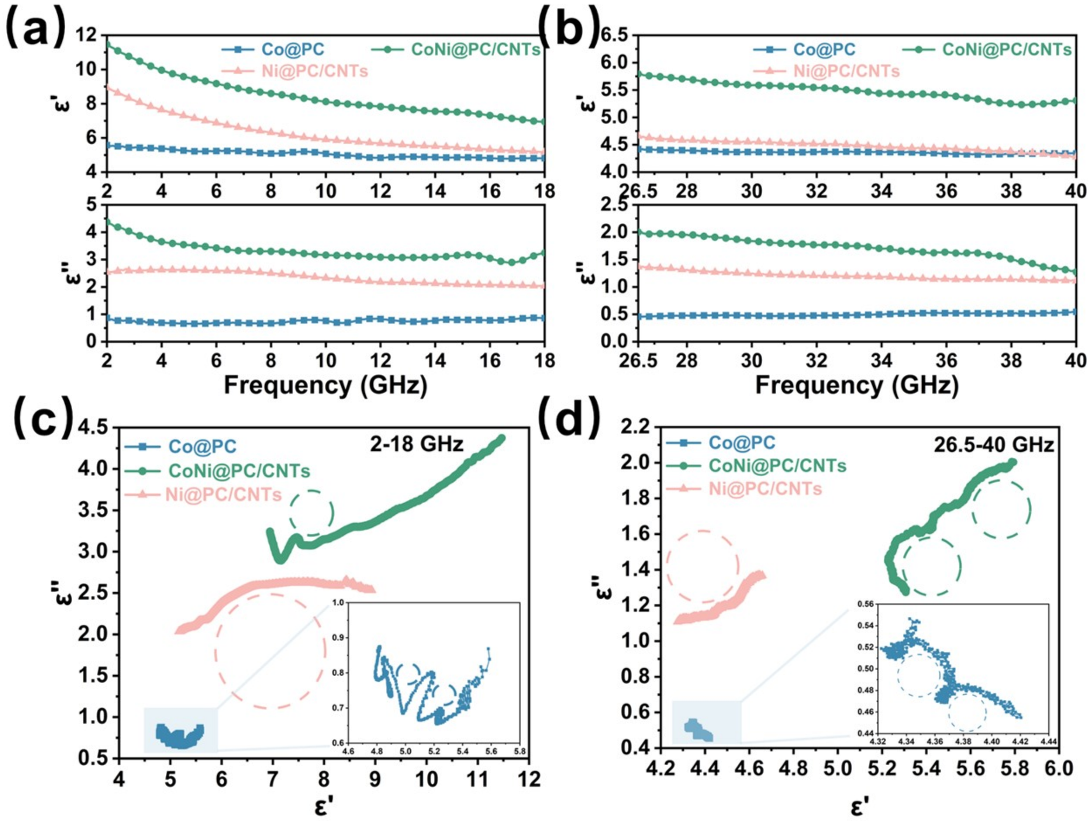

Figure S5. a, b) ε′ and ε″ values, c, d) the Cole–Cole curves of Co@PC, CoNi@PC/CNTs, and Ni@PC/CNTs in the ranges of 2–18 and 26.5–40 GHz, respectively.

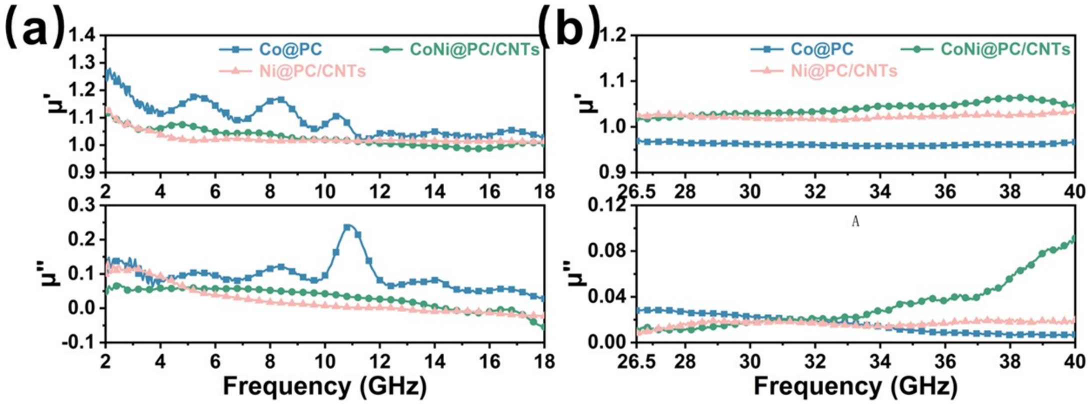

Figure S6. a, b) μ' and μ'' values of Co@PC, CoNi@PC/CNTs, and Ni@PC/CNTs in the ranges of 2–18 and 26.5–40 GHz.

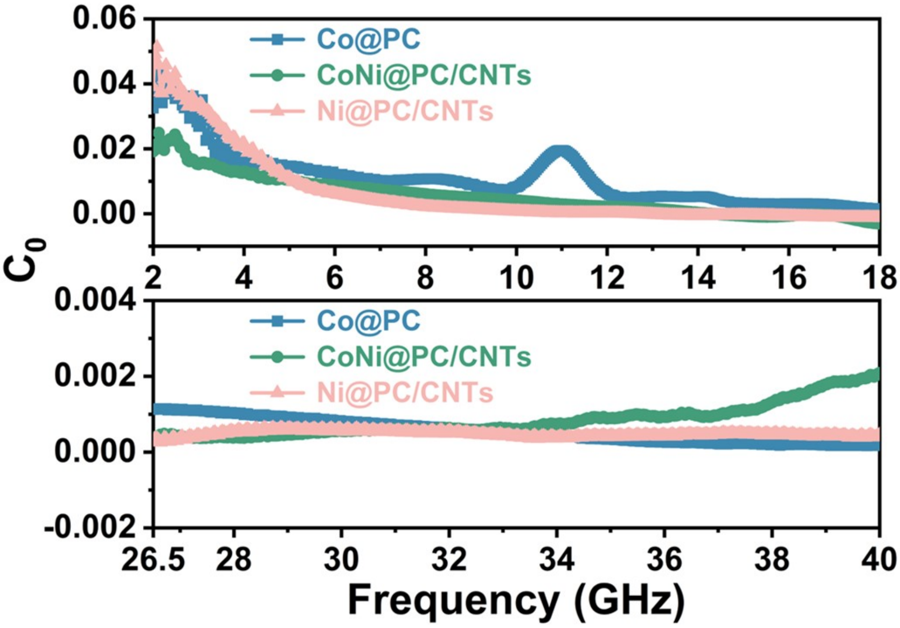

Figure S7. C_0 curves of Co@PC, CoNi@PC/CNTs, and Ni@PC/CNTs in the ranges of 2–18 and 26.5–40 GHz.

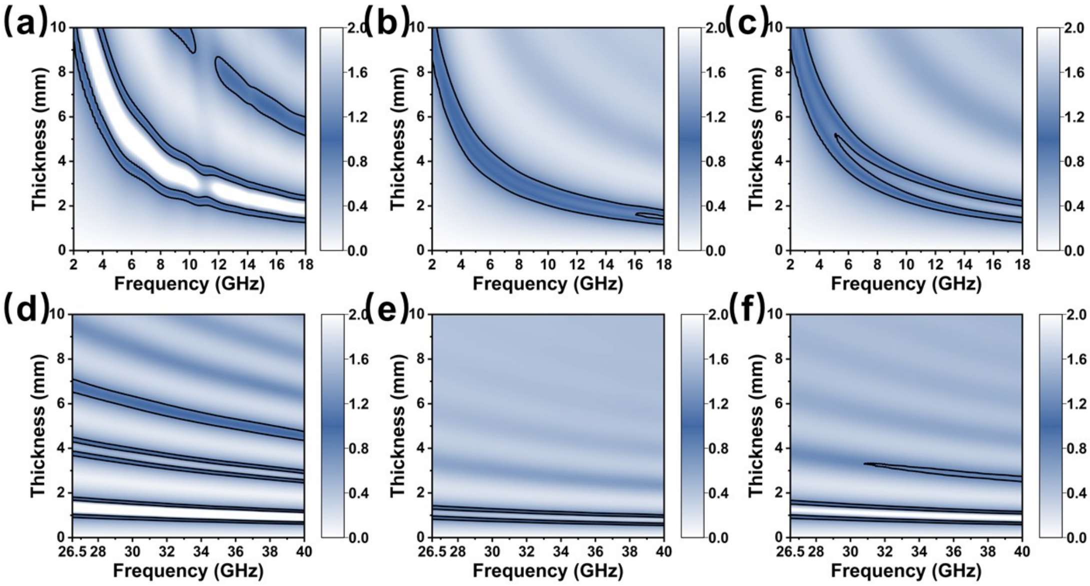

Figure S8. a-f) 2D contour maps $|Z_{in}/Z_0|$ of Co@PC, CoNi@PC/CNTs, and Ni@PC/CNTs in the ranges of 2–18 and 26.5–40 GHz.

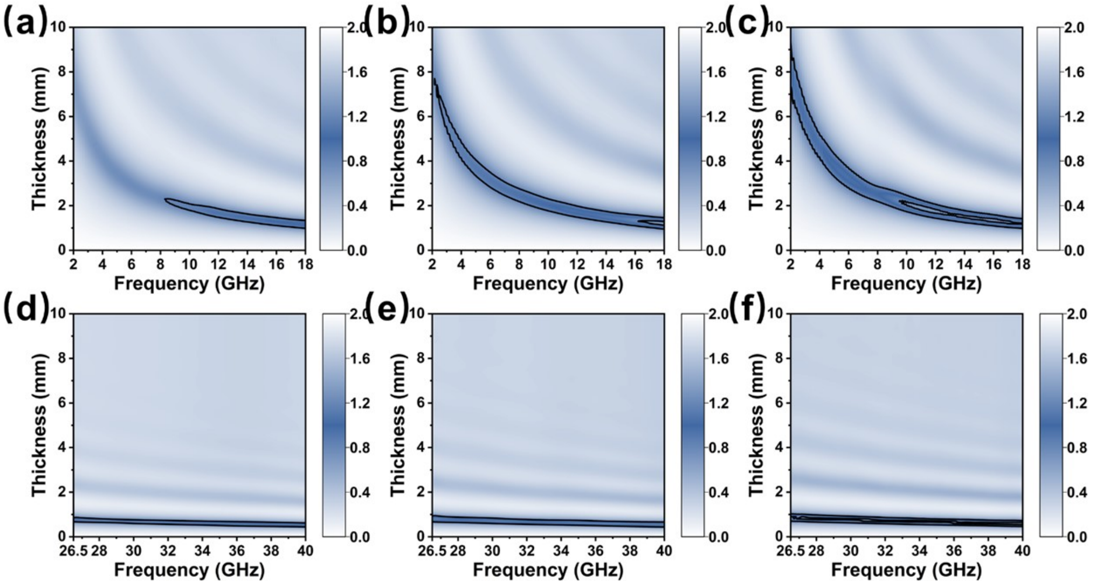

Figure S9. a-f) 2D contour maps $|Z_{in}/Z_0|$ of Co@NPC/NCNTs, CoNi@NPC/NCNTs, and Ni@NPC/NCNTs in the ranges of 2–18 and 26.5–40 GHz.

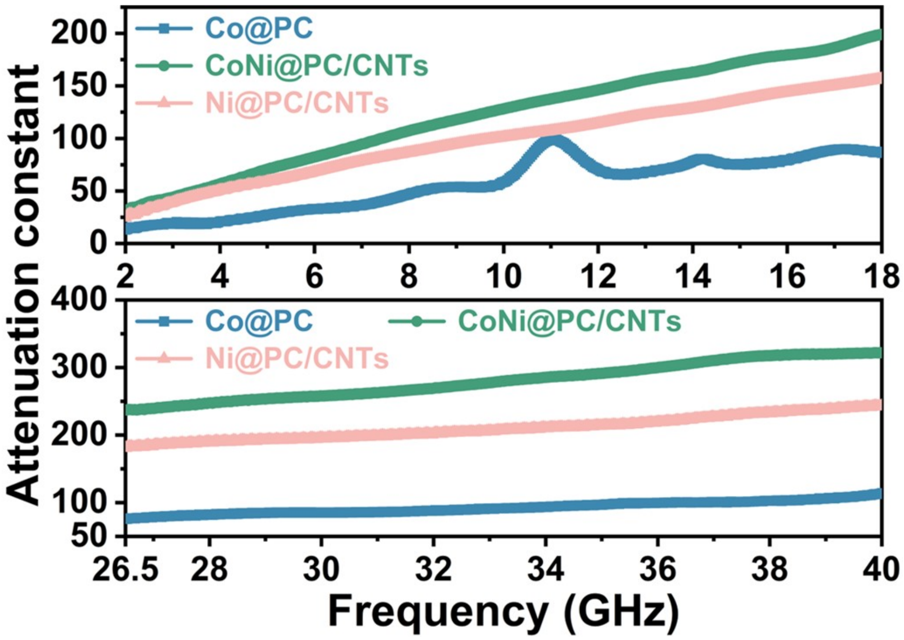

Figure S10. Attenuation constant of Co@PC, CoNi@PC/CNTs, and Ni@PC/CNTs in the ranges of 2–18 and 26.5–40 GHz.

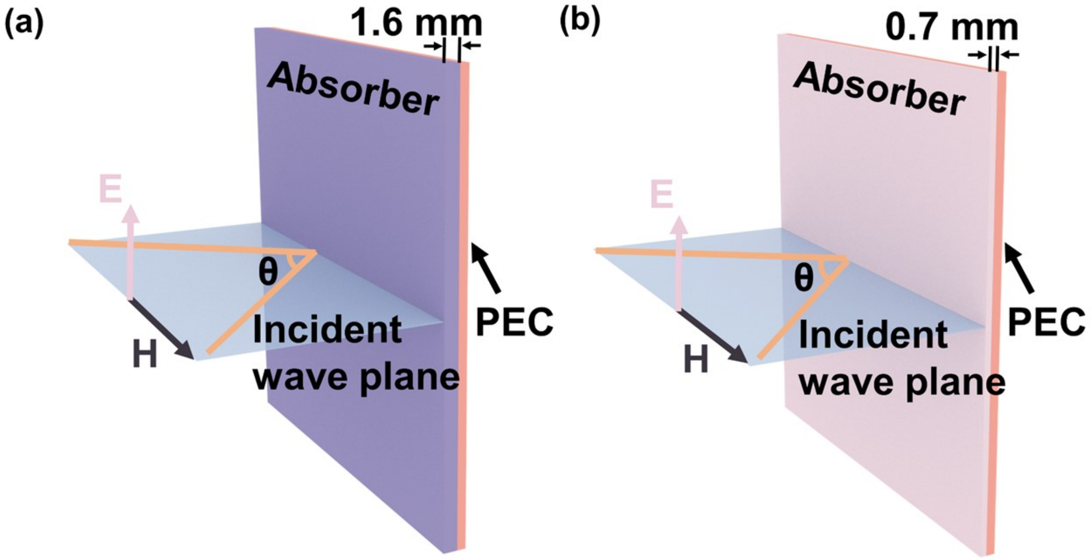

Figure S11. The models of CoNi@NPC/NCNTs and PEC for RCS simulation at 14.16 and 32.81 GHz, respectively.

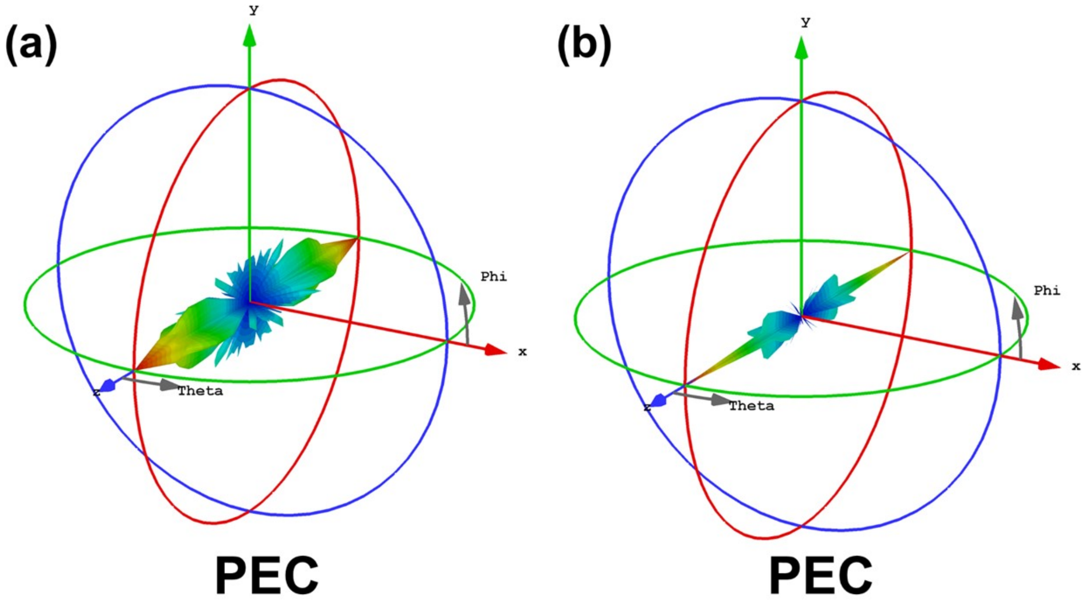

Figure S12. 3D RCS simulation plots of pure PEC at 14.16 and 32.81 GHz, respectively.

References

1. X. Hang, Y. Xue, Y. Cheng, M. Du, L. Du and H. Pang, *Inorg. Chem.*, 2021, **60**, 13168-13176.
2. C. Yu, Y. Wang, J. Cui, D. Yu, X. Zhang, X. Shu, J. Zhang, Y. Zhang, R. Vajtai, Pulickel M. Ajayan and Y. Wu, *J. Mater. Chem. A*, 2018, **6**, 8396-8404.
3. W. Gu, S. J. H. Ong, Y. Shen, W. Guo, Y. Fang, G. Ji and Z. J. Xu, *Adv. Sci.*, 2022, **9**, 2204165.
4. Y. Ren, X. Wang, J. Ma, Q. Zheng, L. Wang and W. Jiang, *J. Mater. Sci. Technol.*, 2023, **132**, 223-251.
5. J. Pan, H. Yang, Q. Hong, H. Wen, J. Q. Xiao and J. Hu, *J. Mater. Chem. C*, 2021, **9**, 7302-7309.
6. H. Wei, Z. Zhang, G. Hussain, L. Zhou, Q. Li and K. Ostrikov, *Appl. Mater. Today*, 2020, **19**, 100596.
7. W. Hou, K. Peng, S. Li, F. Huang, B. Wang, X. Yu, H. Yang and H. Zhang, *J. Colloid Interface Sci.*, 2023, **646**, 265-274.
8. J. Cheng, H. Zhang, M. Ning, H. Raza, D. Zhang, G. Zheng, Q. Zheng and R. Che, *Adv. Funct. Mater.*, 2022, **32**, 2200123.
9. X. Wang, L. Zhang, E. Ding, X. Cao, C. Luo and L. Huang, *Carbon*, 2023, **214**, 118316.
10. H. Xu, B. Li, X. Jiang, Y. Shi, X. Zhang, C. Zhu, X. Zhang and Y. Chen, *Carbon*, 2023, **201**, 234-243.
11. S. Gao, S. Yang, H. Wang, G. Wang, P. Yin and X. Zhang, *Composites, Part B*, 2021, **215**, 108781.
12. C. Zhang, K. Luo, J. Liu, H. Zhang, C. Xu, R. Zhang, Y. Cheng, J. Zhang, L. Wu and R. Che, *J. Mater. Sci. Technol.*, 2024, **175**, 1-9.
13. T. Jia, Y. Hao, X. Qi, Y. Rao, L. Wang, J. Ding, Y. Qu and W. Zhong, J. Mater. Sci. Technol., 2024, **176**, 1-12.
14. J. Liang, Z. Wei, X. Zhang, F. Chen, X. Cao, Z. Li, B. Gao, X. Qi, S. Tang and J. Kong, *Carbon*, 2023, **210**, 118080.

15. Y. Wang, P. Zhao, B. Liang, K. Chen and G. Wang, *Carbon*, 2023, **202**, 66-75.
16. C. Dong, X. Wang, P. Zhou, T. Liu, J. Xie and L. Deng, *J. Magn. Magn. Mater.*, 2014, **354**, 340-344.
17. Y. Chen, X. Fu, L. Liu, Y. Zhang, L. Cao, D. Yuan and P. Liu, *Polym-Plast. Technol. Mater.*, 2018, **58**, 903-914.
18. L. Wang, X. Yu, X. Li, J. Zhang, M. Wang and R. Che, *Chem. Eng. J.*, 2020, **383**, 123099.
19. M. Ning, P. Jiang, W. Ding, X. Zhu, G. Tan, Q. Man, J. Li and R. W. Li, *Adv. Funct. Mater.*, 2021, **31**, 2011229.
20. C. Jiang and B. Wen, *Small*, 2023, **19**, 2301760.
21. Y. Wang, H. Zhang, Q. Wu, S. Li, H. Gao, B. Wan, D. Wen and G. Zeng, *J. Mater. Chem. C*, 2023, **11**, 4171-4181.